Comparison of Acoustic Predictions Using Distributed and Compact Airloads

Matthew Misiorowski PhD Candidate
Farhan Gandhi Redfern Professor and Director
Center for Mobility with Vertical Lift (MOVE), Rensselaer Polytechnic Institute, Troy, New York, USA
Phuriwat Anusonti-Inthra
Aerospace Engineer
U.S. Army Combat Capabilities Development Command, Army Research Laboratory
Aberdeen Proving Ground, Maryland, USA

ABSTRACT

This study examines the performance and acoustics of a co-rotating coaxial rotor in hover with flow simulated using the comprehensive analysis code, RCAS, and high-fidelity CFD/CSD model with Helios. A viscous vortex particle method (VVPM) was used to model the rotor-rotor interference in RCAS. Simulations were conducted at various index angles between the upper and lower rotors. From the results it was observed that the VVPM and Helios simulations both predicted similar trends in rotor performance at various index angles. However, the VVPM simulation predicted generally higher sectional lift at the blade tips compared to the Helios results. Both the VVPM and Helios models were used to predict the acoustic properties of the rotor and the VVPM simulation (compact airloads) was found to over-predict the thickness noise by 1.25 dB at the investigated index angles. Additionally, the VVPM result was within 1 dB of the loading noise predicted by Helios (distributed airloads). In the higher harmonic range (at observer locations directly below the rotor), the VVPM acoustic results are very different than those predicted by Helios. When the index angle is between $-30^o \leq \phi \leq +30^o$, the magnitude of the thickness and loading acoustic pressure waves are largest and the corresponding thickness and loading noise is largest for this range of index angles. As the separation of the blades increases ($|\phi| > 30^o$), the thickness and loading noise tend to decrease. While the thickness noise is primarily generated in-plane (elevation angle 0^o), the loading noise is predominantly at an elevation between 20^o to 50^o.

INTRODUCTION

Rotorcraft acoustics tends to be more noticeable than that of fixed wing aircraft, partly because of lower flight altitudes. With the tremendous recent interest in electric vertical take-off and lading (eVTOL) aircrafts, there are goals to leverage these technologies for various military applications including reconnaissance and resupply missions (Ref. 1). In addition, acoustics will play a key role in community acceptance of these eVTOL technologies for urban air mobility and package delivery services.

Prior studies have used the Ffowcs Williams-Hawkings (FW-H) equations for calculating the propagation of acoustic waves. Gallman developed the Rotor Acoustic Prediction Computer Program (RAPP), to investigate main rotor noise and compared results against the Boeing model 360 DNW/AATMR acoustic pressure (Ref. 2). Shirey et al. validated PSU-WOPWOP, based on Farassat's formulation like the previously validated NASA WOPWOP, against the Higher Harmonic Aeroacoustic Rotor Test (HART I) and XV-15 fly-over test data (Ref. 3). Saetti et al. combined the flight simulation code PSUHeloSim with the acoustic prediction tool PSU-WOPWOP to calculate noise for a given flight trajectory (Ref. 4). Boyd et al. developed the Comprehensive Analytical Rotorcraft Model for Acoustics (CARMA) to develop efficient low-noise rotorcraft. Lastly, Sharma et al. developed an automated coupling between the Rotorcraft Comprehensive Analysis Code (RCAS) and PSU-WOPWOP (Ref. 5).

The majority of the acoustic studies mentioned above use various aerodynamic models to calculate the airloads such as free wake or dynamic inflow. These airloads are then used as compact loads along the quarter chord line to calculate the loading noise sources. The thickness noise is often neglected for these early studies. However, high-fidelity CFD can also be used to determine the source terms of the loading and thickness noise from surface pressure distribution and the geometry of the computational model, but the immense cost of using CFD typically prohibits this tool from being used to calculate the aerodynamic loads early in the design process.

This necessitates the need to understand the difference in acoustic predictions that come from compact loading versus distributed pressure. Currently, there is also interest in novel rotor systems with the potential to reduce rotor noise. The coaxial co-rotating (or stacked) rotor system has been proposed as a new system that can improve rotor efficiency by exploiting favorable aerodynamic interactions between the two rotors. Uehara and Sirohi experimentally compared counter- and co-rotating coaxial rotors to an isolated rotor (Ref. 6). Uehara and Sirohi found a 4% increase in power loading when

Presented at the Vertical Flight Society 75th Annual Forum and Technology Display, Philadelphia, Pennsylvania, USA, May 13–16, 2019.

the lower rotor lagged the upper rotor by 10^o when compared to the traditional counter-rotating coaxial rotor. Finally, Bhagwat modeled counter and co-rotating systems using a free vortex wake model within the Rotorcraft Comprehensive Analysis System (RCAS) (Ref. 7). It was observed that an index angle of -15^o (lower rotor leads upper rotor) produces the most favorable variation in induced inflow and this differs from traditional counter-rotating coaxial rotors that benefit from swirl recovery. Additionally, Bhagwat concluded that the benefits from induced inflow realized by the co-rotating system depend on the location and strength of a blade tip vortex when it encounters another blade. Bhagwat concluded the optimum index angle may vary with the number of blades, vertical separation of the rotors, and the blade loading coefficient of the rotors themselves.

The present study used a viscous vortex particle method (VVPM) to investigate a wide range of index angles for a co-rotating system. A high-fidelity CFD/CSD simulation was also completed at multiple index angles to compare with the VVPM results. The aeromechaics performance of the co-rotating system using computational methods were compared. Additionally, PSU-WOPWOP along with the VVPM and Helios results were used to predict the acoustic properties of the rotor system to determine the optimum index angle for minimum noise generation. Lastly, a comparison was made between the acoustic predictions which use the compact loads from VVPM and distributed pressure surface from Helios.

METHODOLOGY

Stacked Rotor Model

This paper presents the results of a representative stacked rotor system that is of interest to the e-VTOL community for potential acoustic advantages. The configuration in Ref. 6 is adopted for this study. The co-rotating system consists of two rotors (each with two blades), vertically offset by 1 chord length (3 in.), both spinning in the same direction. The lower rotor is phased by an index angle $-90^o \leq \phi \leq +90^o$. A negative index angle indicates that the lower rotor leads ahead of the upper rotor, while a positive index angle implies that the lower rotor lags. Each blade has a 40 in. radius and a constant airfoil cross-section of the Boeing VR-12 profile. The blades have a constant chord of 3 in. and are untwisted. Both rotors in the co-rotating system were trimmed to produce 125 pounds of thrust at a constant RPM of 1795, leaving the collective pitch settings of each rotor as the trim variables. The vertical separation of the rotors and trim procedure differs from the rotor experiments in Ref. 6 as it was hypothesized that reducing the vertical separation of the rotors and enforcing equal blade loads would yield some noise reduction at a specific index angle for this rotor. A diagram of the co-rotating model can be seen in Figure 1.

Computational Method

The co-rotating system was simulated both using RCAS (Ref. 8) with a VVPM inflow model and CFD/CSD simulations using Helios (Ref. 9). The VVPM RCAS model was used to account for interference between the upper and lower rotor that may be difficult to capture with a dynamic inflow or prescribed wake model. Additionally, the VVPM model can be evaluated more quickly than the Helios model thus more design space was explored with VVPM. The Helios simulation was used to validate select cases.

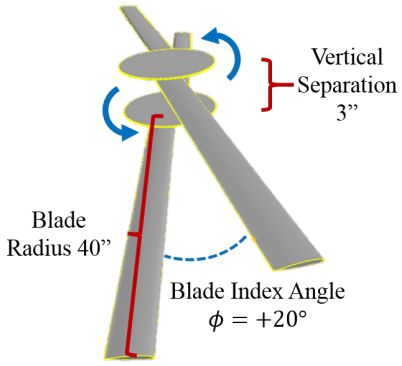

Fig. 1. Stacked rotor geometry setup with negative index angle to show the lower rotor is lagging the upper rotor by 20^o ($\phi = +20^o$)

The comprehensive analysis used in this study is based on a rotorcraft comprehensive code RCAS (version 18.03.C6A) which utilizes multibody dynamic/nonlinear finite element structural analysis to obtain trim solutions and blade deformations. The RCAS model for isolated stacked rotors is shown in Figure 2. The RCAS model consists of two rotors (each with two blades) rotating in the same direction but rotors are offset by an index angle (in Figure 2 the index angle is set to $+20^o$). Each blade is modeled using ten nonlinear beam elements (1D). Twenty-one aerodynamics segments are used to model each blade. Aerodynamic loads are obtained using a table lookup approach and the induced inflow for both rotors is calculated using VVPM. The validation of this method can be found in Ref. 10. Due to the complex interactional aerodynamics between the rotors, lower order aerodynamic models (linear inflow or dynamic inflow) are not suitable. However, the linear inflow model is used to calculate the initial trim parameters and blade deformations.

The rotor is trimmed in hover at sea-level conditions. The trim targets and trim variables are presented in Table 1. Two trim targets/variables are used to trim the stacked rotors; the trim targets are the thrust produced by the upper and lower rotors, with the upper and lower rotor collectives adjusted to achieve these trim targets. After the initial trim variables and blade deformations were calculated, the VVPM inflow model was activated and continued until the converged blade deformation, blade aerodynamic loading, and trim parameters were obtained.

The detailed description of the procedure to couple RCAS and PSU-WOPWOP (a rotorcraft acoustic prediction code) is presented in Ref. 5, and is briefly described here. At the conclusion of the RCAS simulations the blade deformations and loads produced by RCAS are converted into a suitable format to be read into WOPWOP. An appropriate WOPWOP input

file is produced according to the rotor geometry and desired acoustic outputs (observer locations, acoustic pressure, spectrum analysis, etc.). In this study the overall sound pressure level (OASPL), spectrum analysis, and frequency information are recorded at 370 observer locations on a hemisphere below the rotors of radius 33.33 feet (10 rotor radii). The elevation angle of observers ranges from 0^o (in the rotor plane) to 90^o (directly beneath the rotor); a diagram of the elevation angles for the hemisphere of observers can be seen in Figure 3.

Table 1. Trim targets and corresponding trim variables for CA/CSD model

Trim Targets	Trim Variables
Total Thrust (upper rotor) 125 lbs	Upper Rotor Collective Pitch (deg.)
Total Thrust (lower rotor) 125 lbs	Lower Rotor Collective Pitch (deg.)

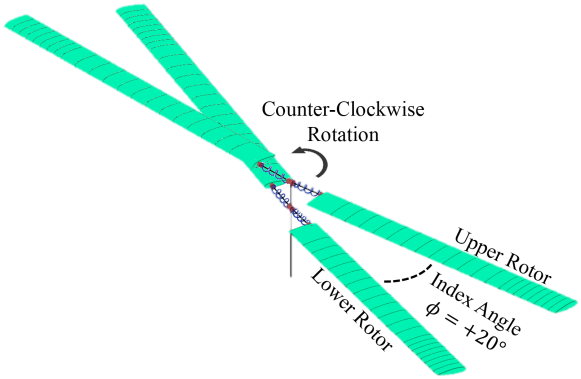

Fig. 2. RCAS model of stacked rotor system with lower rotor lagging by 20^o $(\phi = +20^o)$

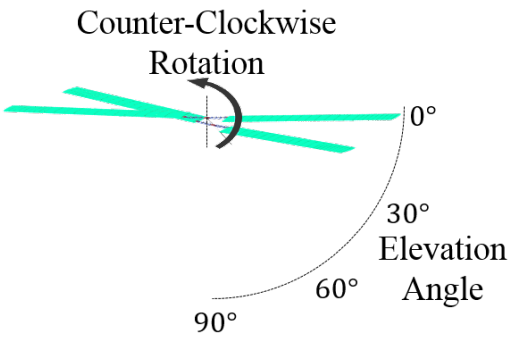

Fig. 3. Diagram of co-rotating system with elevation angles of observers on hemisphere

For the Helios CFD/CSD analysis, an overset grid approach is employed using mStrand and SAMCART as near-body and off-body solvers respectively (Ref. 11). mStrand is a native solver within the Helios framework and solves the Reynolds-Averaged Navier-Stokes (RANS) equations on semi-structured (structured in the wall-normal direction, strands generated from unstructured surface mesh) grids. SAMCART provides flow solutions on the multi-scale Cartesian grid system with adaptive mesh refinement (AMR) capability.

The strand mesh grows from the no-slip walls and uses viscous element spacing ($y+ \leq 1$) at the surface. Up to five strands can be constructed from each point on the surface. A near-body grid system with 21 million grid points has been generated for each rotor with two blades. An image of the near-body mesh used for the blades can been seen in Figure 4.

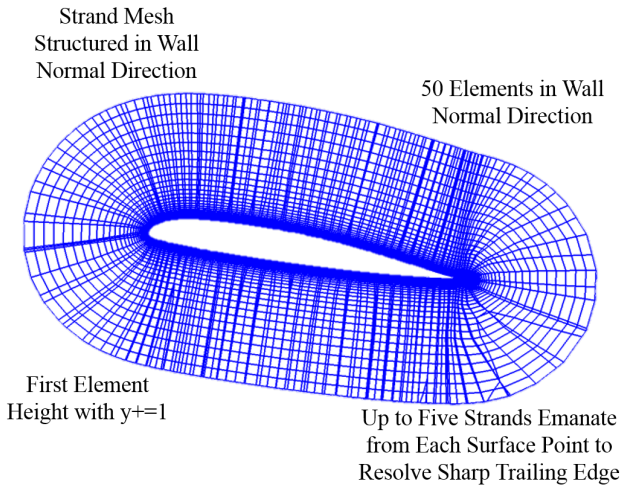

Fig. 4. Cross-section of near-body blade mesh on the rotor blades with 200 points along the top and bottom surface

The off-body Cartesian computational domain extends at least 20 rotor radii in all directions and the off-body mesh employs 8 levels of refinement (each refinement level reduces the grid spacing by half) as well as adaptive mesh refinement to capture vortex structures. The initial off-body mesh consists of 17 million grid points prior to any adaptation. The most refined level of the Cartesian mesh contains elements that are 1/20th the tip chord in size and 53% of the total off-body elements created are in this level of refinement (prior to adaptation).

A means to trim the rotors as well as calculate the structural dynamics of the flexible blade is needed so the Helios solution is coupled to the comprehensive analysis code RCAS. A loose coupling is implemented which initiates after the first three revolutions then each coupling iteration occurs every 180^o of rotation. After each coupling iteration the comprehensive analysis RCAS sends the rotor pitch angle and structural deflections to Helios. The aerodynamic forces calculated in Helios are directly applied to the aerodynamic control points in the RCAS rotor model to calculate the deflections and a new trim state is calculated. Typically, about 14 coupling iterations are required to get converged trim variables.

The physical time step corresponds to 0.25 degrees of rotor rotation. Due to the structured nature of the near- and off-body meshes, the near-body solver was found to reduce the residual by two orders of magnitude with 18 sub-iterations while 12 sub-iterations were required for the off-body solution to reduce the residuals by the same amount. The study employs a Detached Eddy Simulation (DES) with a Spalart-Allmaras (SA) RANS model near the body which is consistent with state-of-the-art computational rotorcraft studies. All simulations were run on DOD HPC Clusters and required between 115,000 to 140,000 core hours for the co-rotating model to achieve a converged solution (12-14 rotor revolutions with about 14 loose coupling iterations).

A tool was developed initially for converting OVERFLOW CFD results into non-compact loading noise sources to be solved in PSU-WOPWOP for noise propagation (Ref. 12). This tool was later adapted by Potsdam to allow unstructured CFD solvers within Helios to couple with PSU-WOPWOP for acoustic analysis (Ref. 13). This code was used in the present study and uses the geometry and surface pressure from the Helios solution to construct the necessary geometry and loading input files for PSU-WOPWOP.

Acoustic analysis of the stacked rotor was completed using PSU-WOPWOP. This Ffwocs Williams-Hawkings (FWH) solver was developed at Pennsylvania State University and can predict discrete frequency and broadband rotor noise. Either through the compact loading provided by RCAS, or the surface pressure calculated by Helios, PSU-WOPWOP determined the loading and thickness noise and propagated them to far away observers. The specified airfoil information from RCAS and the model geometry from Helios were used to determine the thickness noise. Observers were placed in a hemisphere below the co-rotating system and were spaced every 10^o in the azimuthal direction and every 10^o in the elevation direction (going from in the rotor plane to directly below the rotor).

Model Validation

A validation study was completed for both computational methods by comparing the (nondimensional) power loading (C_T/C_P) of the upper and lower rotor to experimental values (Ref. 6) at a range of index angles. The result of the validation study can be seen in Figure 5.

A comparison of C_T/C_P was used due to the difference in trim methodology between Ref. 6 and the present study. Uehara and Sirohi fixed the rotor RPM (1200) and trimmed each rotor to a desired power coefficient ($C_P/\sigma = 0.00845$) as this allowed control over the torque of each rotor on the test stand. The thrust of each rotor was then measured at various index angles. The present study also fixed rotor RPM (1795) and trimmed each rotor to a desired thrust (125 lbs) and calculated the required torque of both the upper and lower rotor in hover.

The upper rotor Helios result closely agrees with the experimental values of C_T/C_P at the four investigated index angles ($+20^o$, 0^o, -20^o, and -40^o), while the Helios slightly overpredicts the performance of the lower rotor compared to the experiment. Both the Helios and experiment predict the upper rotor operates more efficiently (higher C_T/C_P) at index angles $\phi \geq -10^o$. The experiment then outlines a small region of index angles ($-30^o \leq \phi \leq -10^o$) where the lower rotor operates at higher C_T/C_P. The Helios result also predicts for index angles less than -10^o the lower rotor operates at higher C_T/C_P, however, the Helios predicts that region of improved lower rotor efficiency extends past an index angle of -40^o.

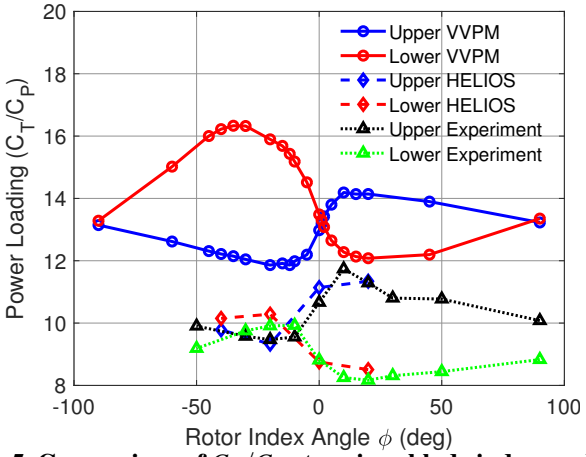

Fig. 5. Comparison of C_T/C_P at various blade index angles for VVPM, Helios, and experiment

The VVPM model under-predicts the required rotor torque compared to both the Helios and experiment but does still capture the trend of the lower rotor operating at higher values of C_T/C_P when at negative index angles. However, the VVPM model predicts the switch in which rotor operates at the higher C_T/C_P occurs at an index angle between 0^o and $+5^o$. Lastly, the VVPM model predicts a much greater difference in the operating C_T/C_P values of the upper and lower rotor for negative index angles than is predicted by Helios or measured by experiment. The underlying cause of this difference will be examined in the Stacked Rotor Aeromechanics section.

RESULTS

Stacked Rotor Aeromechanics

The aerodynamic performance of the co-rotating system was examined using the VVPM and Helios models. The VVPM co-rotating model was run at several index angles but due to the immense computational expense, Helios simulations were only run at $\phi = -40^o$, -20^o, 0^o, and $+20^o$. These index angles were selected to compare with VVPM as this region of index angles showed the greatest variation in the performance of the upper and lower rotor. Figure 6 shows the trimmed values for upper and lower rotor collective pitch (trim variables for each rotor producing 125 lbs thrust) from both the VVPM and Helios simulations.

The Helios simulations predict higher collective pitches (over 1^o) than the VVPM simulation at corresponding index angles. The VVPM simulation predicts that the lower rotor must operate at a higher collective pitch to produce the same thrust at nearly all index angles. This is because the lower rotor operates in larger downwash velocities than the upper rotor. However, the VVPM simulation shows a region between index angle $\phi = -30^o$ to $\phi = -10^o$ where the upper rotor operates at a collective greater than or equal to the lower rotor setting. The Helios simulation at $\phi = -20^o$ predicts an even larger difference between the collective settings of the upper and lower rotors (9.5^o and 8.9^o respectively). The Helios simulation of $\phi = -40^o$ indicates the upper rotor still operates at the higher collective setting.

To understand the cause of the disparity in the rotor collective pitch settings between VVPM and Helios, the radial distribution of blade thrust was plotted for the cases $\phi = +20^o$ and $\phi = -40^o$ in Figure 7 and Figure 8, respectively.

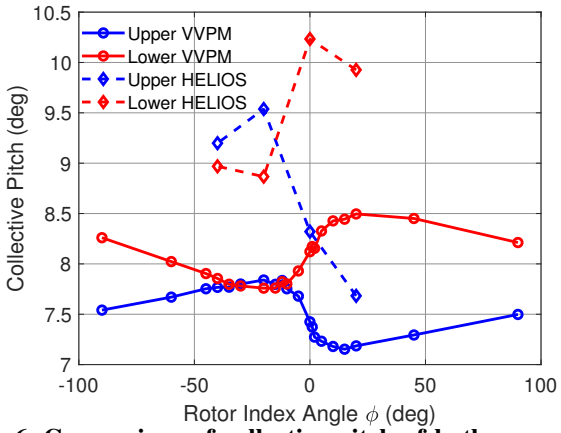

Fig. 6. Comparison of collective pitch of both upper and lower rotors at various blade index angles for VVPM and Helios

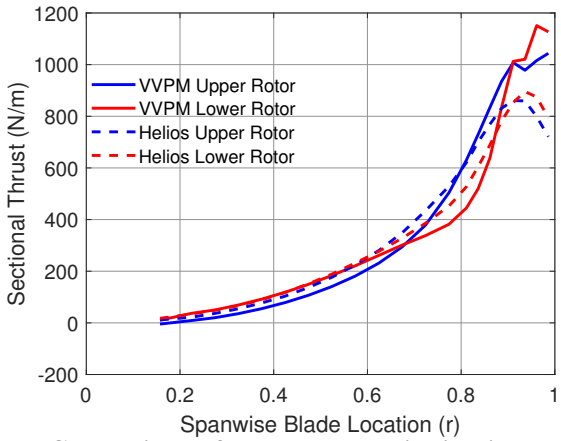

Fig. 7. Comparison of blade thrust distribution at $\phi = +20^o$ for VVPM and Helios

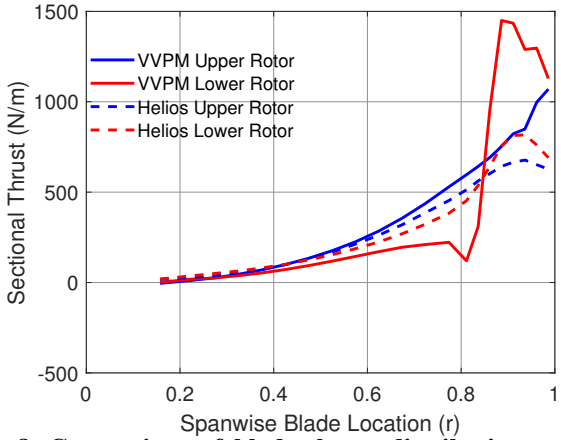

Fig. 8. Comparison of blade thrust distribution at $\phi = -40^o$ for VVPM and Helios

In the case for both index angles, the Helios simulations predict more lift generated inboard on the rotor blade and tip loss causing loss of lift generated outboard. For the VVPM simulations, much more of the blade thrust is generated close to the tip. This indicates the VVPM simulation does not accurately model the tip losses and the induced inflow calculated is different than the flow field calculated by the Helios simulation.

Figure 9 and Figure 10 show the wake structure as calculated by the VVPM and Helios simulations respectively for the $\phi = +20^o$ case.

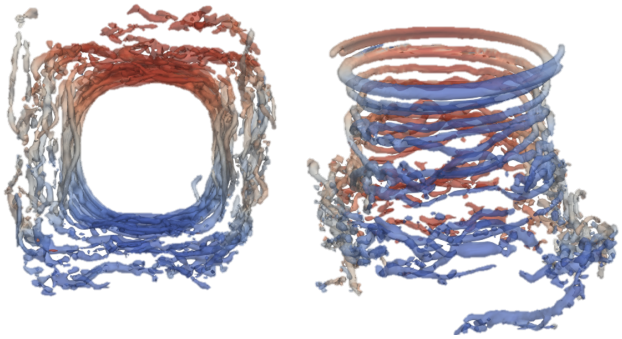

Fig. 9. Isovorticity in the wake (colored by X vorticity) as calculated by VVPM when ϕ =+20^o as seen from the top and side

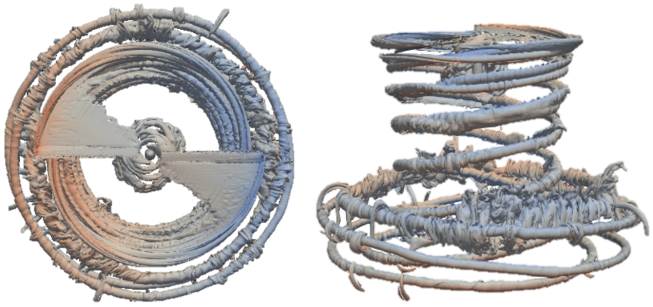

Fig. 10. Isovorticity in the wake (colored by X momentum) as calculated by Helios when ϕ =+20^o as seen from the top and side

The top view of the wake in Figure 9 shows that the VVPM simulation results in a wake that is slightly squared (as compared to the Helios wake in Figure 10) due to differences in the diffusion calculation in the downstream rotor wake. This distortion of the VVPM wake may account for the difference in sectional lift produced at the blade tips in the VVPM simulation.

Stacked Rotor Aeroacoustics

Once an understanding of the aeromechanics was established for the co-rotating system, the acoustic properties of the rotor were examined and compared between the VVPM and Helios simulations. The overall sound pressure level (OASPL)

produced by the rotor system was separated into the thickness and loading noise contributions. The OASPL calculated using PSU-WOPWOP tool uses either the compact, quarter-chord loads from the VVPM simulation or the distributed pressure and geometry from the Helios. The thickness noise calculated from the VVPM and Helios simulations are shown in Figure 11 and Figure 12, respectively, for the case where $\phi = +20^o$ and display the noise over the period of one rotor revolution. Figure 13 shows the difference in dB level between the VVPM and Helios based models. The red and blue disks in the acoustic charts represent the location of the upper and lower rotor respectively.

Figure 11 and Figure 12 show the thickness noise is largest near the rotor plane and is between 80-85 dB at its peak. The difference plot in Figure 13 shows that the thickness noise calculated by the VVPM-RCAS simulation is consistently 1.25 dB higher than calculated from the Helios boundary surfaces of the rotor blades. This difference in thickness noise may stem from the VVPM simulation using a NACA-0012 airfoil (scaled to the correct chord length and rotated by the correct pitch at each section along the blade) versus the Helios simulation using the computational model geometry (VR-12 airfoild with 10.6% thickness).

Similarly, the contribution of loading noise was calculated using the VVPM compact loads and Helios pressure distribution and can be seen in Figure 14 and Figure 15 over the period of a rotor revolution. Figure 16 shows the difference in loading noise between the compact loads produced by RCAS and the distributed pressure produced by Helios.

Figure 14 and Figure 15 show the maximum loading noise occurs at an elevation $\approx 45^o$ below the rotor plane and reaches a peak between 90-95 dB. Furthermore, the in-plane component (at 0^o elevation below the rotor) of the loading noise is > 85 dB which exceeds the in-plane component produced by the thickness noise.

The difference in loading noise, shown in Figure 16, shows close agreement between the loading noise calculated by RCAS and Helios that are within ± 1 dB at all observers below the rotors.

In addition to comparing the OASPL of thickness and loading noise, a frequency analysis was completed to compare the n/rev contributions of the total noise from the co-rotating system. The results can be seen in Figure 17 and an error analysis comparing the VVPM to Helios is presented in Figure 18. For both the VVPM and Helios generated airloads the frequency contributions were calculated at three locations: an elevation angle of 0^o (corresponding to in the rotor plane), 45^o below the rotor plane, and 90^o (directly below the rotor). The sound pressure level was determined by averaging the values from all observers at that elevation level.

Figure 17 shows that at elevation angles of 0^o and 45^o the 2/rev frequency is dominant for both VVPM- and Helios-based models due to the small index angle ($\phi = +20^o$). However, directly below the rotor (elevation angle 90^o) the 4/rev frequency is dominant in both models.

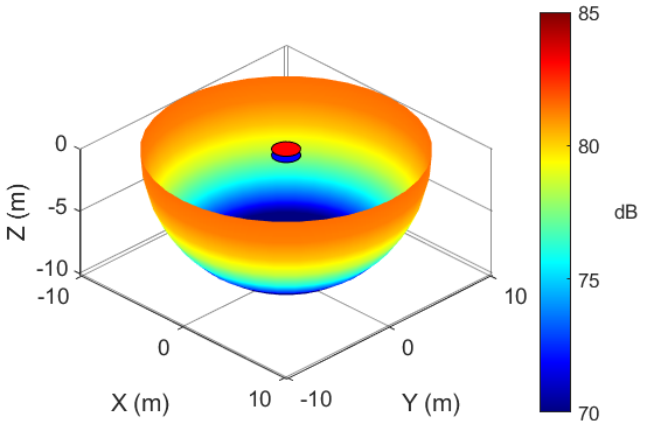

Fig. 11. Thickness noise (dB) below the rotors based on VVPM and comprehensive analysis ($\phi = +20^o$)

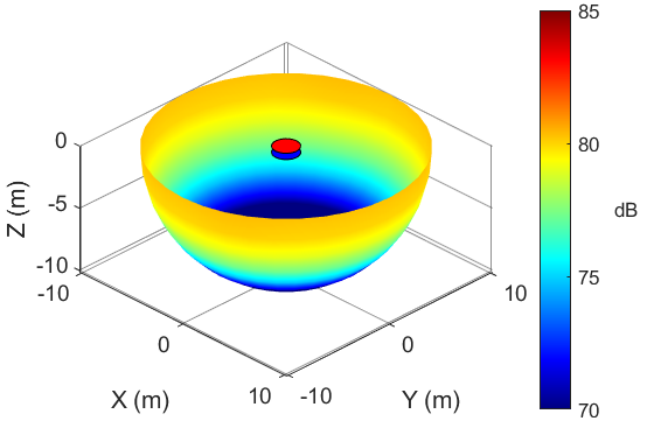

Fig. 12. Thickness noise (dB) below the rotors when using Helios model geometry ($\phi = +20^o$)

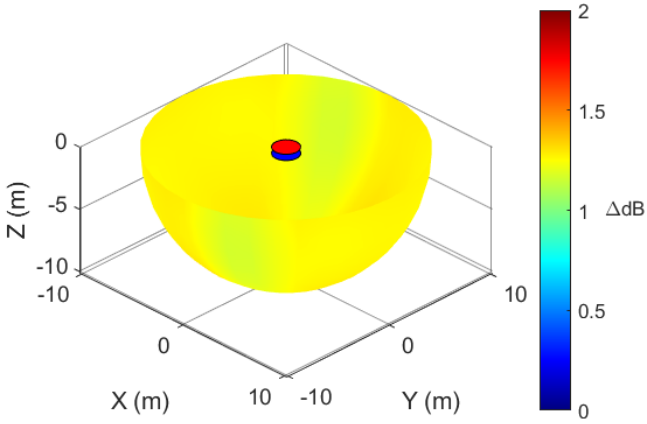

Fig. 13. Difference in thickness noise (ΔdB) below the rotors when subtracting reference Helios based noise from VVPM model ($\phi = +20^o$)

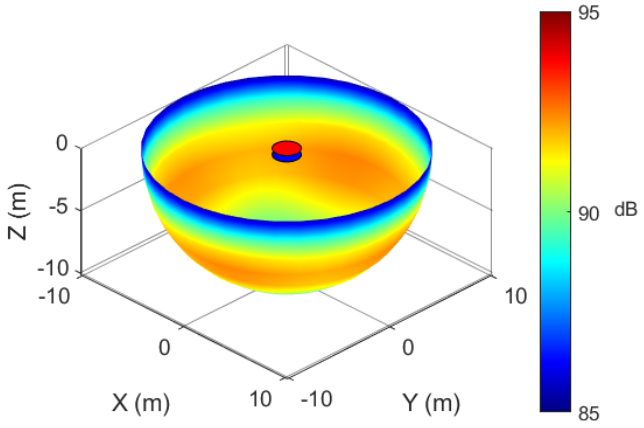

Fig. 14. Loading noise (dB) below the rotors when using VVPM and compact loads ($\phi = +20^o$)

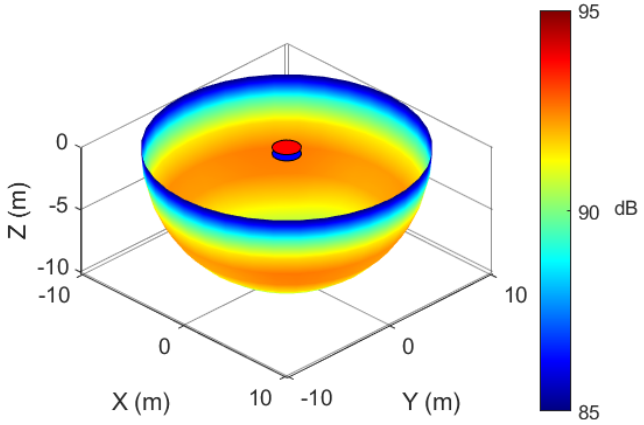

Fig. 15. Loading noise (dB) below the rotors when using Helios and distributed pressure ($\phi = +20^o$)

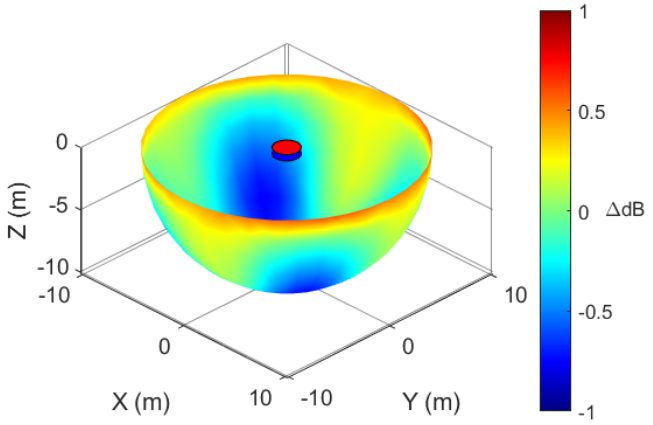

Fig. 16. Difference in loading noise (ΔdB) below the rotors when subtracting reference Helios based noise from VVPM model ($\phi = +20^o$)

In Figure 18, for frequency calculations in the rotor plane (elevation angle 0^o), VVPM under predicts the contribution of the 2/4/6/rev frequencies but agree within 2.75% of the Helios predictions. At an elevation angle of 45^o VVPM and Helios predict similar contributions of the 2/rev and 4/rev frequencies (VVPM predictions within 4% of Helios), however, the VVPM model predicts nearly 23% higher contribution of the 6/rev frequency. Finally, directly below the rotor (elevation angle 90^o) the VVPM-based acoustic prediction compares very poorly with the Helios predictions with -13%, +13%, and +33% differences in the 2/rev, 4/rev, and 6/rev frequencies respectively.

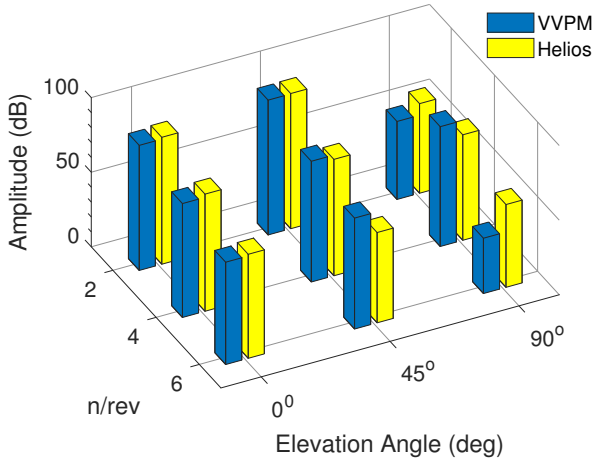

Fig. 17. Comparison of total noise contribution (dB) at different rotor harmonics between VVPM and Helios at various elevation angles ($\phi = +20^o$)

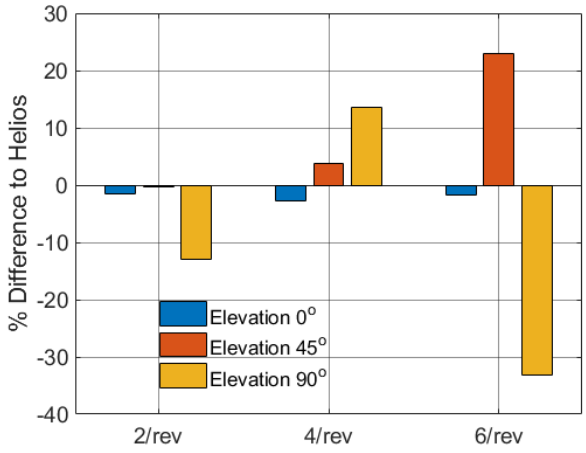

Fig. 18. Percent difference in total noise contribution at different rotor harmonics between VVPM and Helios at various elevation angles ($\phi = +20^o$)

For the case where $\phi = -40^o$ the thickness noise calculated from the VVPM and Helios airloads are shown in Figure 19 and Figure 20 respectively. Figure 21 shows the difference in dB level between the VVPM and Helios based models.

Figure 19 and Figure 20 show the thickness noise in the rotor plane is lower (75 – 80 dB) compared to the $\phi = +20^o$ case. The difference plot in Figure 21, which is consistent with Figure 13, shows that the thickness noise calculated by the VVPM-RCAS simulation is consistently 1.25 dB higher than calculated from the Helios boundary surfaces. This is again likely to RCAS generating the WOPWOP inputs using an assumed NACA 0012 airfoil compared to the VR-12 airfoil from the Helios geometry model.

The contribution of loading noise was calculated for the VVPM and Helios models and can be seen in Figure 22 and Figure 23 respectively. Figure 24 shows the difference in loading noise between the RCAS and Helios models.

Figure 22 and Figure 23 show the maximum loading noise occurs at an elevation angle of $\approx 45^o$ below the rotor plane but the peak noise is smaller than that observed in Figure 14 and Figure 15 ($\phi = +20^o$). Furthermore, as with the $\phi = +20^o$ case, the in-plane component (at 0^o elevation below the rotor) of the loading noise exceeds the in-plane component produced by the thickness noise.

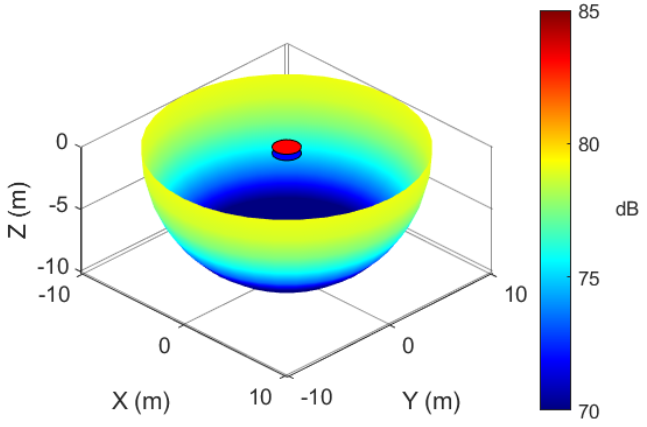

Fig. 19. Thickness noise (dB) below the rotors based on VVPM and comprehensive analysis ($\phi = -40^o$)

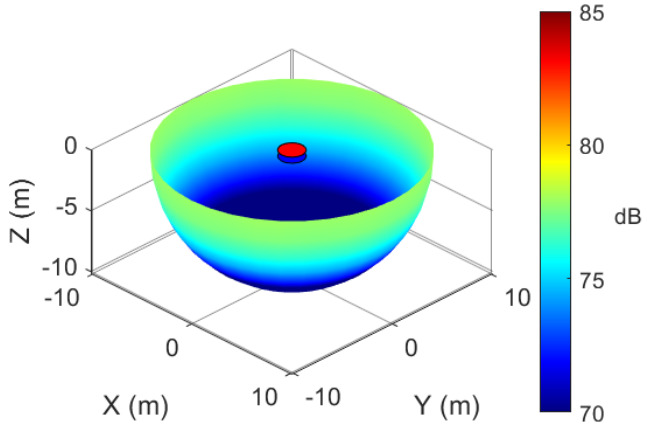

Fig. 20. Thickness noise (dB) below the rotors when using Helios model geometry ($\phi = -40^o$)

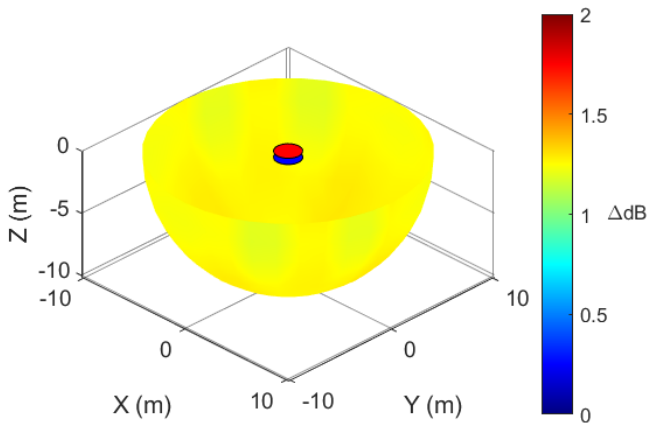

Fig. 21. Difference in thickness noise (ΔdB) below the rotors when subtracting reference Helios based noise from VVPM model ($\phi = -40^o$)

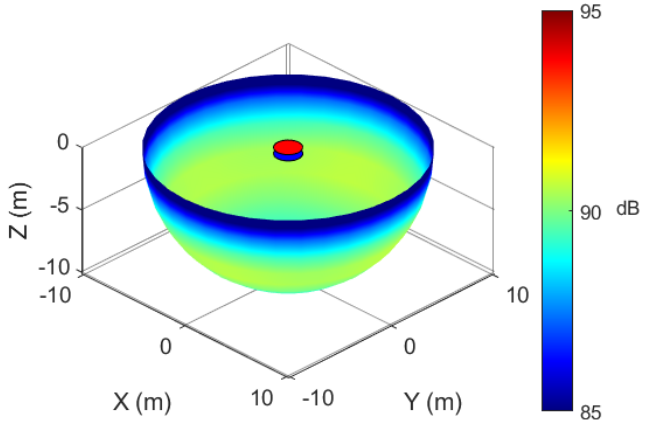

Fig. 22. Loading noise (dB) below the rotors when using VVPM and compact loads ($\phi = -40^o$)

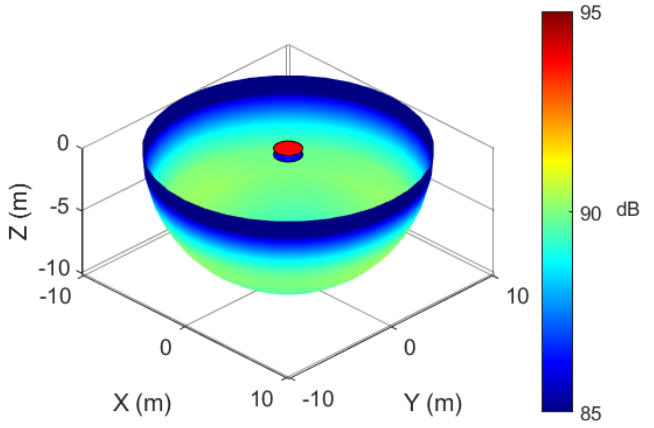

Fig. 23. Loading noise (dB) below the rotors when using Helios and distributed pressure ($\phi = -40^o$)

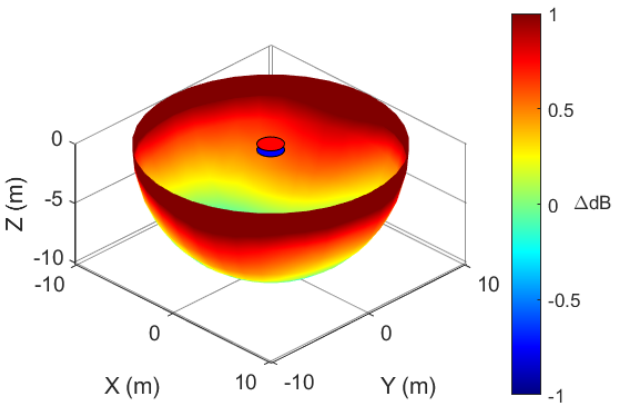

Fig. 24. Difference in loading noise (ΔdB) below the rotors when subtracting reference Helios based noise from VVPM model ($\phi = -40^o$)

The difference in loading noise, shown in Figure 24, shows the RCAS generated airloads predict consistently higher loading noise than Helios but only by less than 1 dB at all observers below the rotors.

The frequency analysis was completed to compare the n/rev contributions of the total noise co-rotating system when $\phi = -40^o$. The results can be seen in Figure 25 and the error analysis in Figure 26.

Similar to the $\phi = +20^o$ configuration, the 2/rev frequency is dominant at elevation angles of 0^o and 45^o. Directly below the rotor (elevation angle 90^o) the 4/rev frequency is dominant in both models which is also consistent with the $\phi = +20^o$ frequency analysis (Figure 17). In the rotor plane (elevation angle 0^o), VVPM under predicts the contribution of the 2/4/6/rev frequencies and only closely agrees with the magnitude of the Helios predicted 2/rev frequency. At an elevation angle of 45^o VVPM and Helios predict similar contributions of the 2/rev and 4/rev frequencies, however, the VVPM model predicts 7.5% higher contribution of the 6/rev frequency. Directly below the rotor (elevation angle 90^o), the VVPM-based acoustic prediction differs from the Helios predictions by 6.7%, 2.7%, and 5.3% differences in the 2/rev, 4/rev, and 6/rev frequencies respectively. Overall, Figure 18 and Figure 26 show that the predicted acoustic levels vary more widely between the VVPM- and Helios-based models at higher frequencies.

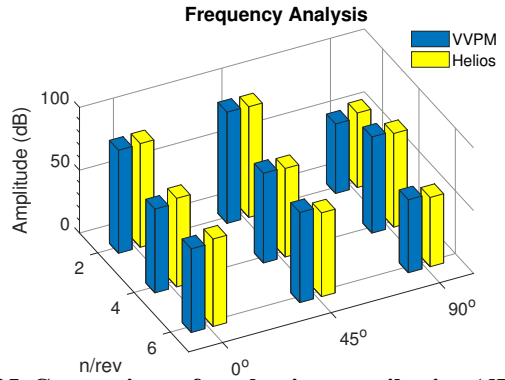

Fig. 25. Comparison of total noise contribution (dB) at different rotor harmonics between VVPM and Helios at various elevation angles ($\phi = -40^o$)

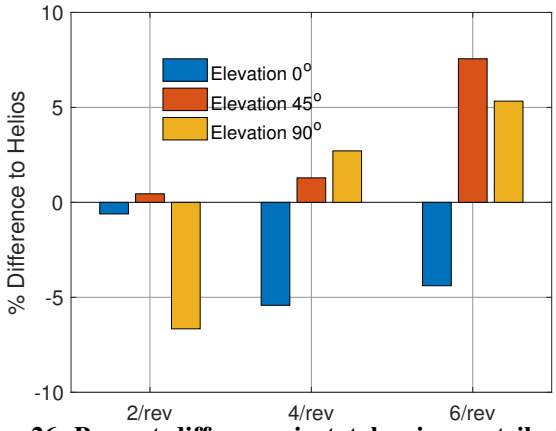

Fig. 26. Percent difference in total noise contribution at different rotor harmonics between VVPM and Helios at various elevation angles ($\phi = -40^o$)

The VVPM model, having compared well with the Helios model in predicting the overall thickness and loading noise, was used to investigate the acoustic pressure associated with the thickness and loading noise at various index angles. Figure 27, Figure 28, and Figure 29 show the instantaneous thickness acoustic pressure for index angles of $\phi = +20^o, 0^o$ and -40^o. Figure 30, Figure 31, and Figure 32 show the instantaneous loading acoustic pressure at the same index angles.

Figure 28 and Figure 31 show that when the index angle ϕ is set to 0^o, the magnitude of both the thickness and loading acoustic pressure reaches peak amplitude and maximized the constructive interference of the acoustic waves. As the index angle moves away from 0^o, the amplitude of the thickness and loading acoustic pressure waves both decrease. Figure 29 shows that when the index angle $\phi = -40^o$ four distinct thickness acoustic pressure waves (two from each rotor) reach the observers over the period of a revolution (compared to the two acoustic waves per revolution as seen in Figure 27 and Figure 28).

The VVPM simulation was used to analyze several index angles $-90^o \leq \phi \leq +90^o$ and the thickness and loading noise was calculated at different elevation angles. The average noise at a specific elevation was taken as the average noise calculated by each observer at the same elevation level. Figure 33 and Figure 34 show the variation of A-weighted sound pressure level at various elevation and rotor index angles for thickness and loading noise respectively.

The thickness noise from Figure 33 shows the highest noise occurs for index angles $-30^o < \phi < +30^o$ and the thickness noise is minimized at index angles of $\phi = \pm 90^o$ (similar to a 4-bladed rotor). The difference in the thickness OASPL is 5 dBA between $\phi = \pm 90^o$ and the moderate index angles ($-30^o < \phi < +30^o$). This increase in thickness noise occurs at all elevation angles.

For the loading noise (Figure 34), the peak OASPL is generated between 20^o and 60^o elevation and at moderate index angles ($-30^o < \phi < +30^o$). The minimum loading noise occurs when the blades have maximum separation $\phi = \pm 90^o$ and is true at all elevation angles.

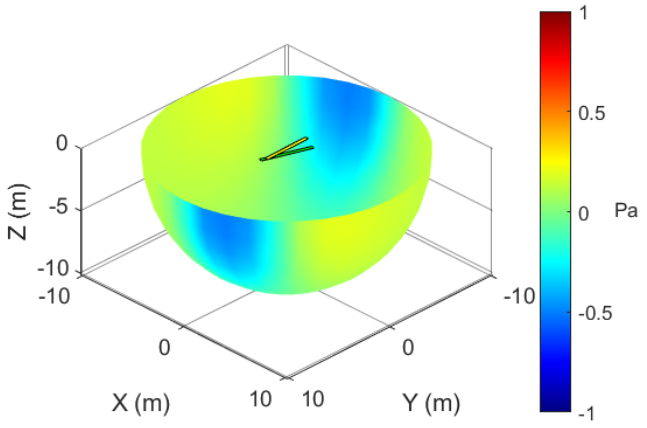

Fig. 27. Thickness acoustic pressure (Pa) below the rotors based on VVPM and comprehensive analysis ($\phi = +20^o$)

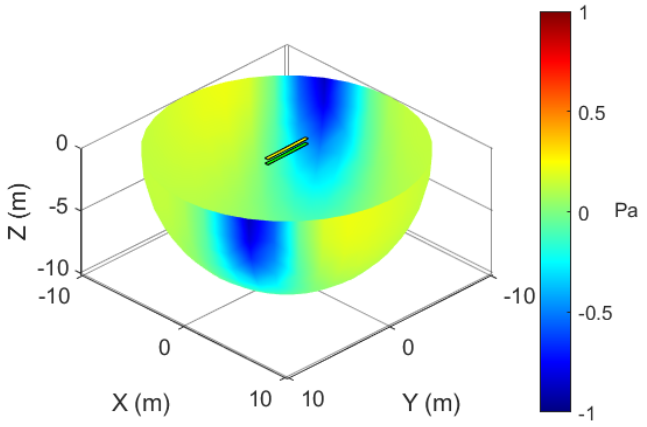

Fig. 28. Thickness acoustic pressure (Pa) based on VVPM and comprehensive analysis ($\phi = 0^o$)

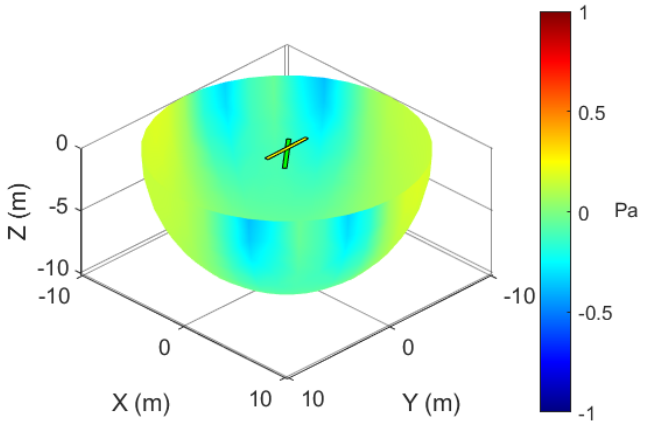

Fig. 29. Thickness acoustic pressure (Pa) based on VVPM and comprehensive analysis ($\phi = -40^o$)

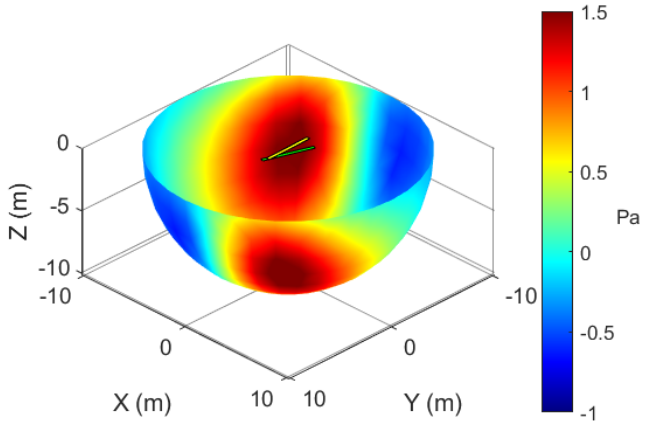

Fig. 30. Loading acoustic pressure (Pa) below the rotors when using VVPM and compact loads ($\phi = +20^o$)

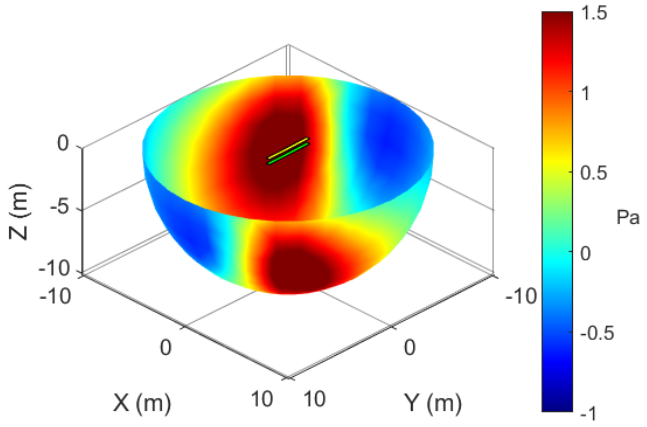

Fig. 31. Loading acoustic pressure (Pa) below the rotors when using VVPM and compact loads ($\phi = 0^o$)

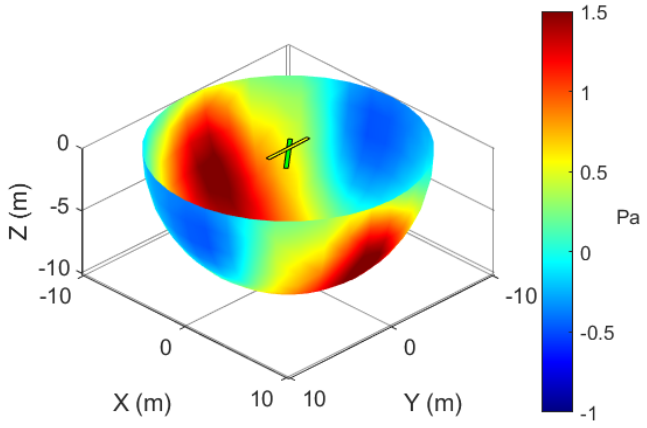

Fig. 32. Loading acoustic pressure (Pa) below the rotors when using VVPM and compact loads ($\phi = -40^o$)

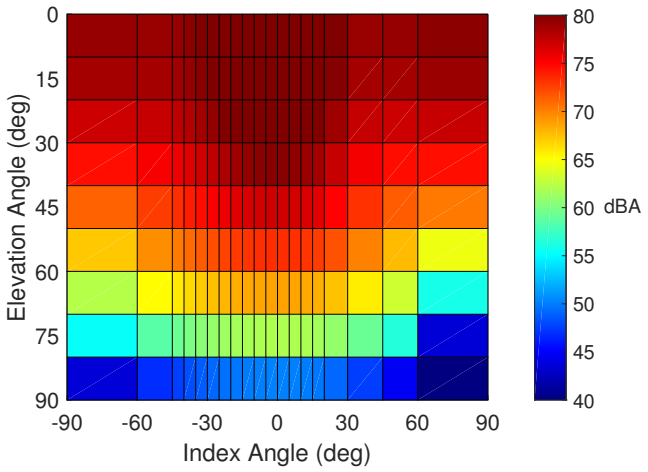

Fig. 33. Thickness noise (dBA) co-rotating index angle vs elevation angle

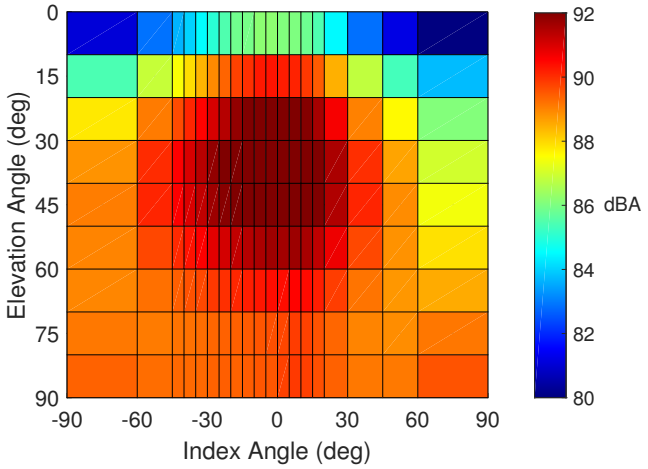

Fig. 34. Loading noise (dBA) co-rotating index angle vs elevation angle

CONCLUSIONS

This study examined the effect of index angles on aerodynamic and aeroacoustic performance of a co-rotating system in hover. Flow field simulations were obtained using RCAS with VVPM inflow model and coupled Helios-RCAS simulations. The rotor speed was fixed at 1795 RPM and the collective pitch of each rotor was varied to trim each rotor to 125 lbs of thrust. From the simulation results the following observations were made.

1. The Helios simulation of the co-rotating system closely agrees with prior experimental results in predicting rotor performance as well predicting the index angles ($-30^o < \phi < -10^o$) where the lower rotor operates at higher C_T/C_P. The VVPM simulation also predicts a range of positive index angles ($-90^o < \phi < 0^o$) where the lower rotor operates at a higher C_T/C_P and similar trends of the rotor performance as index angle is varied. However, the VVPM simulation predicts much higher thrust produced at the blade tips as compared to the Helios results.

2. The thickness noise predicted from the RCAS-based model was consistently 1.25 dB louder than the Helios-based model at all observer locations beneath the rotor for both index angles ($\phi = +20^o$ and $\phi = -40^o$) compared. The loading noise predicted using the compact loads from the VVPM simulation is within 1 dB of the loading noise predicted by Helios at both the investigated index angles.

3. From the frequency analysis completed at $\phi = +20^o$ and -40^o, the 2/rev (associated with the number of blades) is the dominant frequency when the index angle is small. There tends to be poorer agreement between the RCAS- and Helios-based acoustic predictions at the higher frequencies and directly below the rotor (at most 33% difference).

4. At smaller index angles, the dominant acoustic frequency tends to be 2/rev (similar to a two-bladed rotor), while at larger index angles the contribution of the 4/rev frequency increases (similar to a four-bladed rotor).

5. When looking at the VVPM sweep of index angle, the thickness noise is highest between index angles of $-30^o < \phi < +30^o$. The thickness noise in this index angle range is 5 dBA higher than when the index angle is 90^o. Similarly, the loading noise reaches a maximum between index angles $-30^o < \phi < +30^o$ and at an elevation between 20^o and 50^o below the rotor plane.

ACKNOWLEDGMENTS

The first author acknowledges that this research was, in part, sponsored by the Army Research Laboratory and was accomplished under Cooperative Agreement Number W911NF-18-2-0310. The views and conclusions contained in this document are those of the authors and should not be interpreted as representing the official policies, either expressed or implied, of the Army Research Laboratory or the U.S. Government. The U.S. Government is authorized to reproduce and distribute reprints for Government purposes notwithstanding any copyright notation herein.

The authors would also like to thank the High Performance Computing Modernization Program (HPCMP) and the HPC Internship Program (HIP) for providing the funding and resources necessary to complete this study.

Part of this work was carried out at the Rensselaer Polytechnic Institute's Center for Mobility with Vertical Lift (MOVE) with support from the Army/Navy/NASA Vertical Lift Research Center of Excellence (VLRCOE) Program, grant number W911W61120012, with Dr. Mahendra Bhagwat and Dr. William Lewis as Technical Monitors.

Lastly, the authors would like to thank Kalki Sharma for developing the RCAS to WOPWOP tools and his continued work to make said tools applicable to novel rotor systems.

REFERENCES

[1]Freedberg, S., "Army Helicopters: Piecemeal Modernization For Future War," in *Breaking Defense*, 2017.

[2]Gallman, J., "The Validation and Application of a Rotor Acoustic Prediction Computer Program," tech. rep., U.S. Army Aeroflightdynamics Directorate, May 1990.

[3]Shirey, J. S., Brentner, K., and Chen, H., "A Validation Study of the PSU-WOPWOP Rotor Noise Prediction System," tech. rep., 45th AIAA Aerospace Sciences Meeting and Exhibit, Reno, Nevada, USA, Jan. 2007.

[4]Saetti, U., Horn, J., Brentner, K., Villafana, W., and Wachspress, D., "Rotorcraft Simulations with Coupled Flight Dynamics, Free Wake, and Acoustics," AHS Forum 72, West Palm Beach, FL, May 2016.

[5]Sharma, K., Corle, E., Brentner, K., and Anusonti-Inthra, P., "Robust and Automated Coupling of RCAS and PSU-WOPWOP," AHS Aeromechanics Design for Transformative Vertical Flight, 2018.

[6]Uehara, D., and Sirohi, J., "Quantification of Swirl Recovery in a Coaxial Rotor System," AHS International 73rd Annual Forum and Technology Display, Fort Worth, Texas, USA, May 2017.

[7]Bhagwat, M., "Co-rotating and Counter-rotating Coaxial Rotor Performance," AHS Aeromechanics Design for Transformative Vertical Flight, San Francisco, California, USA, Jan. 2018.

[8]Saberi, H., Khoshlahjeh, M., Ormiston, R., A., and Rutkowski, J., J., "Overview of RCAS and Application to Adcanced Rotorcraft Problems," AHS Decennial Specialist's Conference on Aeromechanics, San Francisco, CA, Jan. 2004.

[9]Sitaraman, J. Potsdam, M., Jayaraman, B., Datta, A., Wissink, A., Mavriplis, D., and Saberi, H., "Rotor Loads Predictions Using Helios: A Mulit-Solver Framework for Rotorcraft CFD/CSD Analysis," 49th AIAA Aerospace Sciences Meeting including the New Horizons Forum and Aerospace Exposition, Kissimmee, FL, Jan. 2011.

[10]He, C., and Zhao, J., "Modeling Rotor Wake Dynamics with Viscous Vortex Particle Method," *AIAA Journal*, vol. 47, no. 4, pp. 902–915, 2009.

[11]Wissink, A., Katz, A., Chan, W., and Meakin, R., "Validation of the Strand Grid Approach," 19th AIAA Computational Fluid Dynamics, San Antonio, TX, June 2009.

[12]Boyd, D., "HART-II Acoustic Predictions using a Coupled CFD/CSD Method," AHS 65th Annual Forum, Grapevine, TX, May 2009.

[13]Potsdam, M., Fulton, M., Yeo, H., Ormiston, R., Sim, B., and Dimanlig, A., "Advancing State-of-the-Art Unsteady, Multidisciplinary Rotorcraft Simulations," DoD High Perfornamce Computing Modernization Program Users Group Conference, 2010.